FBMC-based Random Access Signal Design and Detection for LEO Base Stations

Màrius Caus, *Senior Member, IEEE,* and Ana I. Pérez-Neira, *Fellow Member, IEEE*

Abstract—The integration of non-terrestrial networks into the 5G ecosystem is mainly driven by the possibility of provisioning service in remote areas. In this context, the advent of flying base stations at the low Earth orbit (LEO) will enable anywhere and anytime connectivity. To materialize this vision, it is of utmost importance to improve radio protocols with the aim of allowing direct satellite access. Bearing this aspect in mind, we present a new random access signal, which is based on the filter bank multicarrier (FBMC) waveform, and a computationally efficient detection scheme. The proposed solution outperforms the standardized access scheme based on single-carrier frequency division multiplexing (SC-FDM), by reducing out-of-band (OOB) emissions and reducing the missed detection probability in presence of very high carrier frequency offset (CFO), which is inherent to LEO satellite systems. The improvement is related to the fine frequency resolution of the detector and the use of pulse shaping techniques. Interestingly, the FBMC-based random access signal achieves a high level of commonality with 5G new radio, as the preamble generation method and the time-frequency allocation pattern can be kept unchanged. Concerning the practical implementation aspects, the complexity of the detector is similar in both SC-FDM and FBMC.

I. Introduction

THE increasing demand for resilience, capacity and ubiquitous coverage has positioned non-terrestrial networks (NTN) as key infrastructures in the 5G ecosystem. The features of NTN facilitate the development of prominent use cases, such as the connectivity to moving platforms and the provision of broadband services in remote areas. The work presented in this paper focuses the attention on regenerative satellite payloads, where the base station is on board a low Earth orbit (LEO) satellite. Hence, the satellite can be regarded as a flying base station.

The network architecture supports direct and indirect satellite connectivity. In direct and indirect access modes, terminals communicate with the satellite directly and through a relay node, respectively. The relay node can terminate the procedures up to Layer 3 [1]. In the proposed deployment, we favor the option that does not require any terrestrial infrastructure. In such a case, the air interface must be able to overcome the impairments that are inherent to satellite communications. Accordingly, the main challenges that must be faced to allow direct satellite access encompass the long round trip time (RTT) and the high carrier frequency offset

M. Caus is with the Centre Tecnològic de Telecomunicacions de Catalunya (CTTC), 08860 Castelldefels, Barcelona, Spain (e-mail: marius.caus@cttc.cat).

A.I. Pérez-Neira is with the Department of Signal Theory and Communications, Universitat Politècnica de Catalunya (UPC), 08034 Barcelona, Spain and with the Centre Tecnològic de Telecomunicacions de Catalunya (CTTC), 08860 Castelldefels, Barcelona, Spain (e-mail: ana.isabel.perez@upc.edu, ana.perez@cttc.es).

(CFO) that originates from the orbital movement. It is worth highlighting that in LEO satellite systems, the RTT and the CFO considering an Earth fixed equipment, might be up to 40 ms and ±48 KHz, respectively, for a carrier frequency of 2 GHz. These values are significantly higher than those encountered in terrestrial communications [2]. This represents a serious obstacle to integrate 5G new radio (NR) with the satellite technology.

It is noteworthy that if the user equipment (UE) is provisioned with satellite ephemeris and is equipped with a global navigation satellite system (GNSS), which allow compensating the RTT and the CFO, 5G NR can be used over satellite links with a few adjustments. This method is referred to as UE specific pre-compensation. If the GNSS service is not available or the UE is not aware of the satellite's trajectory, the time and the frequency misalignment can still be mitigated to a high extent by performing beam specific pre-compensation and by broadcasting system information in the downlink frames. In such a case, the UE is aware of the minimum RTT in the reference beam and the satellite applies correction mechanisms so that any user located in a given reference point does not experience any CFO. Unfortunately, beam specific pre-compensation techniques yield residual frequency errors when users are not near the reference point. Thus, the higher the beam size, the higher will be the residual errors. If pre-compensation is not performed or if residual errors are still too high, the technical reports elaborated in 3GPP Releases 15 and 16 open the door to enhance the physical random access channel (PRACH) format [1], [3]. The ideas highlighted by 3GPP focus the attention on redesigning the preamble or increasing the subcarrier spacing. The measures suggested to enhance the preamble are based on employing Gold/*m*-sequences or cascading multiple Zadoff-Chu (ZC) sequences.

Following the Release 16 study, NTN have been included in the technical specifications of the 3GPP Release 17. The normative work that is done in Release 17 covers scenarios where the UE has GNSS capabilities, which can be exploited to apply a pre-compensation for the Doppler frequency. For this reason the legacy PRACH waveform and preamble designs have been reused. This paper focuses on more challenging scenarios where the UE cannot pre-compensate the Doppler, requiring PRACH enhancements. In this respect, several works have investigated the preamble design to improve the robustness of the access scheme against the CFO. For instance, the authors in [4], [5] have proposed a novel preamble format that is based on symmetric ZC sequences. Alternatively, in [6], the random access preamble is constructed by employing *m*-sequences. Another solution is presented in [7], where a long sequence structure is obtained by concatenating short

ZC sequences. Remarkably, each sub-sequence is generated from the same root. The scheme has been enhanced in [8] by concatenating the conjugated and circularly shifted replicas of a single root ZC sequence. Performance enhancements are shown in presence of CFOs. It has been recently shown in [9] that the robustness to CFO can also be increased if sub-sequences do not share the same root, that is by constructing a preamble that is made up of multiple different root ZC sequences.

With the aim of exploring innovative solutions that go beyond 5G (B5G) standardization activities, a new random access preamble signal has been proposed in [10], which is based on the pruned discrete Fourier transform (DFT) spread filter bank multicarrier (DFT-s-FBMC) [11]. This FBMC waveform is a modified version of [12]. It deserves to be stated that recent studies endorse FBMC as a potential candidate waveform for future systems [13], [14]. In light of this, the emphasis in [10] is given to the waveform, rather than the preamble sequence, which is the case of [4]–[9]. Therefore, the solution presented in [10] and previous works that address the CFO mitigation from the aspect of the preamble sequence are not exclusive. However, the combination of FBMC with different preamble structures is not tackled in this paper and is deferred to future works. From the standpoint of the waveform, the merits of the FBMC-based preamble design come from the low envelope fluctuation, the good spectral confinement and the robustness to frequency shifts. One of the most advantageous features of DFT-s-FBMC over the commonly used FBMC is the reduction of the tail overhead. This characteristic allows the DFT-s-FBMC waveform to transmit the PRACH sequence defined in 5G NR in the same time and frequency resources specified in the standard [15]. This is fundamental to achieving a high degree of commonality with 5G NR. However, the proposed design does not fit into the specifications of the Release 17, which employs the single-carrier frequency division multiplexing (SC-FDM) waveform to generate the PRACH. It is worth emphasizing that practical implementation and performance aspects have not been examined with sufficient thoroughness in [10]. The novelty of the paper in these two aspects are briefly explained in the following.

One example that reveals that practicality has not received its due attention in [10] lies in the fact that the implementation of the proposed receiver is very demanding in terms of computational effort. The complexity burden comes from the adoption of the sliding window approach. The idea is to use multiple windows with the same duration as the preamble signal. Each window has a different time lag to cover all possible delays within the random access channel. In each window, a preamble search is performed. This entails feeding the selected samples into the analysis filter bank (AFB) and then, correlating the outputs with a set of locally generated sequences. The AFB is employed to recover the symbols conveyed on each subcarrier. Remarkably, the application of the sliding window technique implies executing multiple times the AFB and the preamble detector. Clearly, this is not efficient. Ideally, we would like to use a single window and execute the AFB and the preamble detector just once. Towards this end, a new preamble structure is required, which has motivated

this work. The new design has to guarantee that regardless of the delay, the receiver is able to find a fixed window that captures all the necessary preamble samples to successfully perform the preamble detection. The key feature that allows us to reduce the complexity of the detector and thus, making the pruned DFT-s-FBMC more appealing to become the PRACH waveform, is the circularity. The most common approach to obtain a circular structure is to transmit redundancy in the form of a cyclic prefix (CP). To preserve the good frequency localization properties of the pruned DFT-s-FBMC waveform, the CP cannot be directly generated by appending the last samples ahead of the signal. This is due to the overlapping structure of FBMC-like schemes. Alternatively, the CP must be built in the frequency domain. This is a distinctive feature of the proposed design.

To improve the RACH performance, we have investigated signal processing techniques to optimize the detection of the preamble. To accomplish this goal we focus on ensuring that the received preamble preserves the good correlation properties of the transmitted preamble. To guarantee that the pruned DFT-s-FBMC scheme does not alter the structure of the transmitted preamble, the time-reversal technique must be applied, both at the transmitter and the receiver. The time-reversal operation is crucial to achieve phase continuity across subcarriers and across multicarrier symbols. Without phase continuity, pseudo correlation peaks may emerge, yielding detection errors. The application of the time-reversal technique to the pruned DFT-s-FBMC modulation is an innovative aspect that boils down to a matrix permutation operation, which hardly contributes to the computational complexity increase.

In order to simplify the interpretation of the random access signal generation, the placement of the CP and the application of the time-reversal technique can be regarded as a pre-processing step that transforms the preamble sequence. First, a periodic extension of the preamble sequence is created. Next, a segment of the periodic sequence is arranged into a two-dimensional grid. The size of the segment is a design parameter. Finally, the rows of the two-dimensional matrix are reversed. Remarkably, each column of the resulting matrix is a symbol vector that is modulated onto a pruned DFT-s-FBMC waveform.

The new preamble signal described in this paper paves the way to implementing a computationally efficient detector. The proposed detector is based on finding the correlation peaks that exceed a noise dependent threshold and then storing the corresponding timing indexes. This scheme, which is referred to as the traditional method, offers a good trade-off between complexity and performance. To improve the resilience to CFO, alternatives to the traditional method are available in the literature, e.g., [16], [17]. Unfortunately, these solutions do not preserve the excellent correlation properties of the ZC sequence and thus, they suffer from serious performance degradation at low SNR. To mitigate the noise, the preamble sequence must be modified as the authors propose in [8]. Since the paper focuses on the waveform design, we stick to the traditional detection method and the preamble sequences specified in 5G NR [15]. The objective of the work presented in this paper is to reinforce the FBMC-based access scheme

suitability in highly mobile environments, such those that result from deploying flying base stations. More specifically, the major contributions of the paper are summarized as follows:

- Propose a new random access signal that is based on the pruned DFT-s-FBMC waveform and allows fast preamble detection. The proposed signal exhibits good time and frequency localization and low envelope fluctuation. In addition, it achieves a high level of commonality with 5G NR.
- Design a computationally efficient preamble detector that is tailored to the characteristics of the new preamble. The implementation complexity lies in computing the point-wise multiplication with the local ZC root sequence, executing the inverse fast Fourier transform (IFFT) algorithm and performing the peak search. Interestingly, the size of the IFFT controls the frequency resolution.
- In comparison to the standardized access scheme based on SC-FDM, the devised FBMC-based solution reduces out-of-band (OOB) emissions, detects the presence of the transmitted preamble with similar complexity and reduces the missed detection probability (MDP) in presence of very high CFO.

The rest of the paper is organized as follows. In Section II we formulate the system model. Next, Section III characterizes the channel and evaluates the impact of time and carrier frequency offsets. Leveraging the analysis conducted in Section III, sections IV and V respectively describe the preamble design and the preamble detection. Finally, the numerical results are presented in Section VI and the conclusions are drawn in Section VII.

Notation: Upper- and lower-case boldface letters denote matrices and vectors, respectively. Let the superscripts $(.)^T$, $(.)^*$ and $(.)^H$ denote, respectively, transpose, complex conjugate and Hermitian transpose operations. We will use $[\mathbf{A}]_{ij}$ to refer to the (i, j)-th element of a matrix $\mathbf{A}$. By $\mathbf{I}_N$ we denote the N-th order identity matrix. The $M \times N$ all-zeroes matrix is denoted $\mathbf{0}_{M \times N}$. We define $\lfloor x \rceil$ and $\lfloor x \rfloor$ to be the nearest integer to x and the greatest integer less than or equal to x, respectively. diag $(\mathbf{a})$ is a diagonal matrix with the entries of the vector $\mathbf{a}$ on its diagonal. $\sqrt{-1}$ is denoted by j. The sets of $N \times M$ real- and complex-valued matrices are respectively denoted by $\mathbb{R}^{N \times M}$ and $\mathbb{C}^{N \times M}$.

II. SYSTEM MODEL

It must be underlined that in satellite communications the multipath effect is usually weak. For this reason we adopt the additive white Gaussian noise (AWGN) channel model to characterize the satellite link. Therefore, the detrimental effects induced by the environment include the time offset (TO) τ, the CFO ϵ and the channel coefficient h. Previous works have made similar assumptions, e.g. [9], [10]. As for the notation, $\tau \in \mathbb{N}$ is normalized to the sampling period T_s and $\epsilon \in \mathbb{R}$ is normalized to the subcarrier spacing Δ_f. According to this model, the received signal is given by $y[n] = hs[n-\tau]e^{j\frac{2\pi}{M}\epsilon n} + w[n]$, where $s[n]$ is the random access signal and $w[n]$ is the

additive noise. The satellite channel obeys the model proposed by [18], [19], namely,

$$h = \sqrt{\frac{G_R G_T}{L K_B T B_{\text{PRACH}}}} e^{j\frac{2\pi}{\lambda} d_{\text{SAT-UE}}}. \quad (1)$$

The magnitude of the channel depends on the satellite antenna gain G_R, the UE antenna gain G_T, the free space loss L, the Boltzmann constant K_B, the bandwidth B_{PRACH} and the system noise temperature T. The phase phase term is function of the carrier wavelength λ and the slant range between the satellite and the UE $d_{\text{SAT-UE}}$. Since the channel is normalized to the noise power, $w[n]$ is a circularly symmetric complex Gaussian random variable with unit variance.

The rest of the section is devoted to model the input-output relation when the random access signal corresponds to an FBMC-like waveform in the form of

$$s[n] = \sum_{k=0}^{N_c+L_{\text{CP}}-1} \sum_{m=0}^{M_a-1} x_m[k]p\left[n - k\frac{M}{2}\right] e^{j\frac{2\pi}{M}m\left(n-k\frac{M}{2}\right)}, \quad (2)$$

where $x_m[k]$ denotes the symbol transmitted on the m-th subcarrier and k-th time instant. In the proposed setup, a subset of M_a out of M subcarriers is allocated to the PRACH. Another important feature of the system is that the pulse shaping process is carried out by the real-valued and low-pass band filter $p[n]$. Without loss of generality, the system employs unitary energy pulses. When pruned DFT-s-FBMC is the waveform of choice to convey the random access preamble, it is of utmost importance to reduce as much as possible the tail overhead. Otherwise, the burst may not fit into the PRACH slot. For this reason, the pulse length is kept to the minimum, i.e. $L = M$. Interestingly, the design of short filters is not incompatible with sidelobe suppression [20].

It is worth highlighting that the new random access signal is composed of two parts: the CP and the preamble sequence. The rationale for transmitting the CP is to reduce the complexity of the preamble detector. Due to the overlapping structure of FBMC-like schemes, the CP cannot be a replica of the time-domain FBMC waveform. Otherwise, the good frequency localization properties are destroyed. Alternatively, the CP must be built in the frequency domain. In (2), the CP and the preamble sequence are transmitted in the multicarrier symbols indexed by $k = 0, \cdots, L_{\text{CP}}-1$ and $k = L_{\text{CP}}, \cdots, N_c + L_{\text{CP}}-1$, respectively. This means that the preamble sequence is split into N_c vector symbols and that the CP spans L_{CP} vector symbols. In Section IV we address the CP design with the aim of ensuring circularity of the preamble at the receiver, which is crucial to allow fast preamble detection.

At the other end of the link, the received signal $y[n]$ is fed into the AFB. To simplify the notation, we initial assume that the delay does not exceed one symbol period, i.e., $0 \le \tau < \frac{M}{2}$. The general case is treated in Section III. In this sense, the demodulated signal at the q-th subcarrier and k-th time instant can be compactly expressed as

$$
\begin{aligned}
z_q[k] &= \sum_n y[n]p\left[n - k\frac{M}{2}\right] e^{-j\frac{2\pi}{M}q\left(n-k\frac{M}{2}\right)} \\
&= \sum_{l=-1}^{1} \sum_{m=0}^{M_a-1} e^{j\pi\epsilon k} x_m[k-l]g_{qm}[l] + w_q[k],
\end{aligned} \quad (3)
$$

for $0 \le q \le M_a - 1$ and $L_{CP} \le k \le L_c + N_{CP} - 1$. Notice that the CP is discarded at receiver. Let $w_q[k]$ denote the filtered noise. The impulse response between the m-th and the q-th subcarrier signal is formulated as

$$
\begin{aligned}
g_{qm}[l] &= \alpha_{qm}[l] e^{j\pi ml} e^{-j\frac{2\pi m\tau}{M}} \\
&= \sum_n e^{j\frac{2\pi\epsilon}{M}n} p[n] p\left[n - \tau + l\frac{M}{2}\right] \times \\
&\quad e^{j\frac{2\pi}{M}n(m-q)} e^{j\pi ml} e^{-j\frac{2\pi m\tau}{M}}.
\end{aligned}
\tag{4}
$$

Although the PRACH occupies M_a subcarriers, $g_{qm}[l]$ and $\alpha_{qm}[l]$ are defined for $0 \le q, m \le M - 1$. The immediate consequence of setting the prototype pulse length to $L = M$ is that only two symbols contribute to inter-symbol interference (ISI), i.e. $-1 \le l \le 1$. If we stack column-wise the demodulated signals as $\mathbf{z}[k] = \left[z_0[k], \cdots, z_{M_a-1}[k]\right]^T$, we get

$$
\mathbf{z}[k] = h \sum_{l=-1}^{1} \mathbf{G}[l]\mathbf{x}[k - l] + \mathbf{w}[k].
\tag{5}
$$

To obtain this matrix notation we have defined the symbol vector $\mathbf{x}[k] = \left[x_0[k], \cdots, x_{M_a-1}[k]\right]^T$ and the noise vector $\mathbf{w}[k] = \left[w_0[k] \cdots w_{M_a-1}[k]\right]^T$. To characterize the interplay between the transmit and the receive subcarrier signals, we build the matrix

$$
\mathbf{G}[l] = \begin{bmatrix} \alpha_{00}[l] & \alpha_{01}[l] & \cdots & \alpha_{0(M_a-1)}[l] \\ \vdots & \vdots & \ddots & \vdots \\ \alpha_{(M_a-2)0}[l] & \alpha_{(M_a-2)1}[l] & \cdots & \alpha_{(M_a-2)(M_a-1)}[l] \\ \alpha_{(M_a-1)0}[l] & \alpha_{(M_a-1)1}[l] & \cdots & \alpha_{(M_a-1)(M_a-1)}[l] \end{bmatrix} \boldsymbol{\beta}_l^\tau.
\tag{6}
$$

The matrix $\mathbf{G}[l]$ is factorized as the product of a Toeplitz matrix by the diagonal matrix

$$
\boldsymbol{\beta}_l^\tau = \mathrm{diag}\left(\left[1, e^{j\frac{2\pi}{M_a}\left(l\frac{M_a}{2} - \tau\frac{M_a}{M}\right)1}, \cdots, e^{j\frac{2\pi}{M_a}\left(l\frac{M_a}{2} - \tau\frac{M_a}{M}\right)(M_a-1)}\right]\right).
\tag{7}
$$

The (q, m)-th entry of the Toeplitz matrix corresponds to $\alpha_{qm}[l]$, which is defined in (4). It is important to remark that $\boldsymbol{\beta}_l^\tau$ stems from a misalignment of $l\frac{M}{2} - \tau$ samples between the transmit and the receive pulses. Assuming that M_a is sufficiently large and that the prototype pulse exhibits good frequency localization, the Toeplitz matrix can be approximated to a circulant matrix. The same approximation has been made in [10], [11]. Relying on this feature, we can factorize $\mathbf{G}[l]$ as function of the DFT matrix $\mathbf{F}_{M_a} = \left[\omega_0, \cdots, \omega_{M_a-1}\right]^T$, namely,

$$
\mathbf{G}[l] = \mathbf{F}_{M_a}^H \boldsymbol{\Xi}_l \mathbf{F}_{M_a} \boldsymbol{\beta}_l^\tau = \mathbf{F}_{M_a}^H \mathrm{diag}\left(\left[\xi_0^l, \cdots, \xi_{M_a-1}^l\right]\right) \mathbf{F}_{M_a} \boldsymbol{\beta}_l^\tau.
\tag{8}
$$

The m-th column of the DFT matrix is defined by

$$
\omega_m = \frac{1}{\sqrt{M_a}}\left[e^{-j\frac{2\pi}{M_a}m0}, \cdots, e^{-j\frac{2\pi}{M_a}m(M_a-1)}\right]^T.
\tag{9}
$$

The channel eigenvalues are gathered in the main diagonal of

$$
\boldsymbol{\Xi}_l = \mathrm{diag}\left(\left[\xi_0^l, \cdots, \xi_{M_a-1}^l\right]\right).
\tag{10}
$$

The circulant approximation imposes that $\alpha_{(M_a-q)0}[l] = \alpha_{(M-q)0}[l]$, for $q = 1, \cdots, M_a/2$. By computing the DFT of $\left[\alpha_{00}[l], \cdots, \alpha_{(M_a/2-1)0}[l], \alpha_{(M-M_a/2)0}[l], \cdots, \alpha_{(M-1)0}[l]\right]$, we can define the channel eigenvalues as

$$
\begin{aligned}
\xi_m^l &= \sum_n e^{j\frac{2\pi}{M}n\epsilon} p[n] p\left[n - \tau + l\frac{M}{2}\right] \times \\
&\quad \frac{\sin\left(\pi\left(\frac{M_a}{M}n + m\right)\right)}{\sin\left(\frac{\pi}{M_a}\left(\frac{M_a}{M}n + m\right)\right)} e^{j\frac{\pi}{M_a}\left(\frac{M_a}{M}n + m\right)}.
\end{aligned}
\tag{11}
$$

Under perfect synchronization conditions, i.e. $\tau = \epsilon = 0$, the eigenvalues become

$$
\lambda_m^l = \sum_n p[n] p\left[n + l\frac{M}{2}\right] \frac{\sin\left(\pi\left(\frac{M_a}{M}n + m\right)\right)}{\sin\left(\frac{\pi}{M_a}\left(\frac{M_a}{M}n + m\right)\right)} e^{j\frac{\pi}{M_a}\left(\frac{M_a}{M}n + m\right)}.
\tag{12}
$$

If we focus the attention on the pruned DFT-s-FBMC signal generation, then it follows that the symbols are precoded at each channel access. The precoded symbol vector can be expressed as

$$
\mathbf{x}[k] = \boldsymbol{\Theta}\mathbf{C}\mathbf{P}\mathbf{d}[k],
\tag{13}
$$

where the data symbol vector is defined by $\mathbf{d}[k] = \left[d_0[k], \cdots, d_{M_a/2-1}[k]\right]^T$. We will show in the following that the linear processing performed in (13) is of key significance to restore the complex orthogonality. It is worth noticing that the pre-processing stage consists in combining three channel matrices. In the first place the power is allocated to the symbols according to the matrix $\mathbf{P} = \mathrm{diag}\left(\left[\sqrt{P_0}, \cdots, \sqrt{P_{M_a/2-1}}\right]\right)$. Next, the symbols are precoded with the pruned DFT matrix $\mathbf{C} = \left[\omega_{M_a-1}, \cdots, \omega_{M_a/2}\right]$. Finally, the matrix $\boldsymbol{\Theta} = \mathrm{diag}\left(\left[e^{j\frac{\pi}{2}0}, \cdots, e^{j\frac{\pi}{2}(M_a-1)}\right]\right)$ is used to introduce a phase shift equal to $\pi/2$ between adjacent symbols. At the other end of the link, the same processing must be performed but in reverse order. Accordingly, we filter the demodulated signal $\mathbf{z}[k]$ by the decoding matrix $\mathbf{A}^H = \mathbf{P}\mathbf{C}^H\boldsymbol{\Theta}^H$, leading to

$$
\mathbf{y}[k] = \mathbf{A}^H\mathbf{z}[k] = he^{j\pi\epsilon k} \sum_{l=-1}^{1} \mathbf{H}_T[l]\mathbf{d}[k - l] + \mathbf{A}^H\mathbf{w}[k].
\tag{14}
$$

The composite channel $\mathbf{H}_T[l]$ results from the combined effects of the DFT processing, the frequency multiplexing, the pulse shaping and the propagation channel. The channel seen by the input vectors is given by

$$
\mathbf{H}_T[l] = \mathbf{P}\mathbf{C}^H\boldsymbol{\Theta}^H\mathbf{F}_{M_a}^H\boldsymbol{\Xi}_l\mathbf{F}_{M_a}\boldsymbol{\beta}_l^\tau\boldsymbol{\Theta}\mathbf{C}\mathbf{P},
\tag{15}
$$

for $l = \{-1, 0, 1\}$. The beauty of the pruned DFT-s-FBMC scheme is that in the absence of time and frequency offsets, i.e. $\tau = \epsilon = 0$, if the power is allocated inversely with the channel eigenvalues as follows

$$
\mathbf{P} = \mathrm{diag}\left(\left[\sqrt{\frac{1}{\lambda_{M_a/4+1}^0}}, \cdots, \sqrt{\frac{1}{\lambda_{3M_a/4}^0}}\right]\right),
\tag{16}
$$

then it follows that $\mathbf{H}_T[0] = \mathbf{I}_{\frac{M_a}{2}}$ and $\mathbf{H}_T[1] = \mathbf{H}_T[-1] = \mathbf{0}_{\frac{M_a}{2} \times \frac{M_a}{2}}$. In addition, as the noise samples at the input of the receiver are zero-mean circularly symmetric complex Gaussian

random variables with unit variance, then it follows that the (q, m)-th entry of the noise covariance matrix is given by $\mathbb{E}\{w_q[k]w_m^*[k]\} = \sum_n |p[n]|^2 e^{-j\frac{2\pi}{M}(q-m)n}$. Analogously to the reasoning in the definition of (8), for large M_a, the covariance matrix can be factorized as

$$\mathbb{E}\{\mathbf{w}[k]\mathbf{w}[k]^H\} = \mathbf{F}_{M_a}^H \mathrm{diag}\left(\left[\lambda_0^0, \cdots, \lambda_{M_a-1}^0\right]\right)\mathbf{F}_{M_a}. \quad (17)$$

Bearing this result in mind, it can be verified that $\mathbf{A}^H\mathbf{w}[k]$ follows a distribution $\mathcal{CN}\left(\mathbf{0}, \mathbf{I}_{\frac{M_a}{2}}\right)$.

III. CHANNEL CHARACTERIZATION

The objective of this section is to demonstrate several desirable properties of the composite channel formulated in (15). Ideally, matrices $\{\mathbf{H}_T[-1], \mathbf{H}_T[0], \mathbf{H}_T[1]\}$ should have at most one non-zero entry in each row and column and all non-zero entries should have constant magnitude. The validity of these properties ensure that the symbols are not distorted, which is of paramount importance to simplify the detection. To have a better understanding of the composite channel, we have extended the analysis conducted in [10] by making a more thorough evaluation of the adverse effects caused by the TO and the CFO. The main difference lies in the fact that no assumptions are made about the relation between M and M_a. In this general case, $\tau\frac{M_a}{M}$ can be decomposed as the sum of its integer and fractional parts, yielding $\tau\frac{M_a}{M} = \tau_I + \tau_f$ with $\tau_I = \lfloor\tau\frac{M_a}{M}\rceil$ and $|\tau_f| \leq 0.5$. In the following we will show that τ_I and τ_f are key parameters in the modelling of the FBMC-based access scheme. For the sake of the analytical tractability we initially bound the maximum delay to the symbol period, so that $0 \leq \tau < \frac{M}{2}$. We will bring back this issue at the end of this section to address the general case where $\tau \geq \frac{M}{2}$.

A. Adverse effects caused by the TO

In this section we characterize the TO, which is parameterized by τ_I and τ_f. However, to obtain manageable mathematical expressions, in some cases it is assumed that $\tau_f = 0$. The most relevant result can be summarized in the following proposition.

Proposition 1: If $\tau_f = 0$, matrices $\{\mathbf{H}_T[-1], \mathbf{H}_T[0], \mathbf{H}_T[1]\}$ have at most one non-zero entry in each row and column. To prove it, we first derive

$$\mathbf{C}^H\mathbf{\Theta}^H\mathbf{F}_{M_a}^H = \left[\mathbf{0}_{\frac{M_a}{2}\times\frac{M_a}{4}+1} \quad \mathbf{I}_{\frac{M_a}{2}} \quad \mathbf{0}_{\frac{M_a}{2}\times\frac{M_a}{4}-1}\right] \quad (18)$$

$$\mathbf{F}_{M_a}\beta_l^\tau\mathbf{\Theta}\mathbf{C} = \left[\omega_{l\frac{M_a}{2}-\tau\frac{M_a}{M}+\frac{M_a}{4}}, \cdots, \omega_{l\frac{M_a}{2}-\tau\frac{M_a}{M}-3\frac{M_a}{4}+1}\right]^H \times \left[\omega_{M_a-1}, \cdots, \omega_{M_a/2}\right]. \quad (19)$$

Now if we plug (18) and (19) into (15), the equivalent channel becomes

$$\mathbf{H}_T[l] = \mathrm{diag}\left(\left[\xi_{\frac{M_a}{4}+1}^l, \cdots, \xi_{\frac{3M_a}{4}}^l\right]\right)\mathbf{P}\mathbf{A}_\tau^l\mathbf{P}, \quad (20)$$

where $\mathbf{A}_\tau^l \in \mathbb{C}^{\frac{M_a}{2}\times\frac{M_a}{2}}$ is a Toeplitz matrix. It can be shown by straightforward calculations that the (q, m)-th element of $\mathbf{A}_\tau^l$ can be expressed as

$$\left[\mathbf{A}_\tau^l\right]_{qm} = \frac{1}{M_a}\frac{\sin\left(\pi\left(m-q-|l|\frac{M_a}{2}-\tau_I-\tau_f\right)\right)}{\sin\left(\frac{\pi}{M_a}\left(m-q-|l|\frac{M_a}{2}-\tau_I-\tau_f\right)\right)}\times \frac{e^{j\pi\left(m-q-|l|\frac{M_a}{2}-\tau_I-\tau_f\right)}}{e^{j\frac{\pi}{M_a}\left(m-q-|l|\frac{M_a}{2}-\tau_I-\tau_f\right)}}, \quad (21)$$

for $m, q = 0, \cdots, \frac{M_a}{2} - 1$. It can be resolved that the fractional part induces inter-carrier interference (ICI). It is noteworthy to mention that significant interference mainly leaks from a small neighbourhood around the frequency of interest. Interestingly, for $\tau_f = 0$ we can recast $\mathbf{A}_\tau^l$ as

$$\mathbf{A}_\tau^0 = \begin{bmatrix} \mathbf{0}_{\frac{M_a}{2}-\tau_I\times\tau_I} & \mathbf{I}_{\frac{M_a}{2}-\tau_I} \\ \mathbf{0}_{\tau_I} & \mathbf{0}_{\tau_I\times\frac{M_a}{2}-\tau_I} \end{bmatrix} \quad (22)$$

$$\mathbf{A}_\tau^1 = \mathbf{A}_\tau^{-1} = \begin{bmatrix} \mathbf{0}_{\frac{M_a}{2}-\tau_I\times\tau_I} & \mathbf{0}_{\frac{M_a}{2}-\tau_I} \\ \mathbf{I}_{\tau_I} & \mathbf{0}_{\tau_I\times\frac{M_a}{2}-\tau_I} \end{bmatrix}. \quad (23)$$

This concludes the proof of Proposition 1. Clearly, the integer part shifts the symbol vectors τ_I positions. More precisely, the first $\frac{M_a}{2} - \tau_I$ positions of $\mathbf{y}[k]$ are occupied by the last $\frac{M_a}{2} - \tau_I$ symbols of $\mathbf{d}[k]$. In addition, the last τ_I vacant positions of $\mathbf{y}[k]$ are filled in with the first τ_I symbols of $\mathbf{d}[k - 1]$ and $\mathbf{d}[k + 1]$.

B. Adverse effects caused by the CFO

The effect of the CFO arises in the eigenvalues of the channel. Upon thoroughly analyzing (11) and (12), we write the following proposition.

Proposition 2: If $\epsilon << M_a/10$, then the channel eigenvalues can be approximated as

$$\xi_m^l \approx e^{j2\pi\epsilon}e^{-j\frac{2\pi}{M_a}m\epsilon}p[n_m]p\left[n_{m+\tau_I}+l\frac{M}{2}\right]M \quad (24)$$

$$\lambda_m^l \approx p[n_m]p\left[n_m+l\frac{M}{2}\right]M, \quad (25)$$

where $n_m = M - \lfloor m\frac{M}{M_a}\rceil$.

Note that the CFO causes a phase rotation to the eigenvalues. The assumptions that have been made to derive (24) and (25) are provided in Appendix A. To confirm the accuracy of the approximations made in Proposition 2, we have computed ξ_m^l, for $M_a = 420$, $M = 1024$ and $\epsilon = 2$. The pulse is designed following the guidelines of the time-frequency localization criterion [20], [21]. Therefore, the coefficients of the pulse are computed as

$$p[n] = \begin{cases} \cos(\pi/2(1-d)) + \gamma_0 t + \\ 2t(t^2-1)(\beta_1 + 4\beta_2 t^2)) & 0 \leq n \leq M/2 - 1 \\ p[M-n-1] & M/2 \leq n \leq M - 1, \end{cases} \quad (26)$$

with $d = (2n + 1)/M$ and $t = 2d - 1$. The coefficients γ_0, β_1 and β_2 are defined in [20]. Comparing the approximation with respect to the exact value, we have observed that the mean

absolute percentage error (MAPE) of the magnitude and the phase is 1.9% and 0.6%, respectively, for $0 \leq \tau < \frac{M}{2}$, $-1 \leq l \leq 1$ and $\frac{M_a}{4} + 1 \leq m \leq \frac{3M_a}{4}$. In light of these results, from here onwards (24) and (25) will be assumed as the true expressions.

Based on the findings of Proposition 2, we can assert the following statement.

Proposition 3: If Proposition 2 remains true, then $\mathbf{H}_T[-1] = \mathbf{0}_{\frac{M_a}{2} \times \frac{M_a}{2}}$, for $0 \leq \tau_I < \frac{M_a}{2}$.

Appendix B includes the derivation steps that lead to the proof of Proposition 3. If we compile Propositions 1 and 3, we can express the received signal as

$$\mathbf{y}[k] = h e^{j\pi k} \mathbf{D}_T \left(\mathbf{A}_\tau^0 \mathbf{d}[k] + \mathbf{A}_\tau^1 \mathbf{d}[k-1] \right) + \mathbf{A}^H \mathbf{w}[k], \quad (27)$$

where the equivalent channel matrix becomes

$$\mathbf{D}_T = \text{diag}\left(\left[\frac{\xi_{\frac{M_a}{4}+1}^0}{\sqrt{\lambda_{\frac{M_a}{4}+1+\tau_I}^0 \lambda_{\frac{M_a}{4}+1}^0}}, \cdots, \frac{\xi_{3\frac{M_a}{4}-\tau_I}^0}{\sqrt{\lambda_{3\frac{M_a}{4}}^0 \lambda_{3\frac{M_a}{4}-\tau_I}^0}}, \right. \right.$$
$$\left. \left. \frac{\xi_{3\frac{M_a}{4}-\tau_I+1}^1}{\sqrt{\lambda_{\frac{M_a}{4}+1}^0 \lambda_{3\frac{M_a}{4}-\tau_I+1}^0}}, \cdots, \frac{\xi_{3\frac{M_a}{4}}^1}{\sqrt{\lambda_{\frac{M_a}{4}+\tau_I}^0 \lambda_{3\frac{M_a}{4}}^0}} \right] \right). \quad (28)$$

To conclude the channel characterization, we provide one of the most important outcomes of the analysis.

Proposition 4: Assuming that (24) and (25) hold with strict equality and that $\tau_f = 0$, then it follows that all non-zero entries of $\mathbf{D}_T$ have constant magnitude.

The mathematical details of Proposition 4 are developed and described in Appendix C. In light of Proposition 4, the received symbol vector becomes

$$\mathbf{y}[k] = h e^{j2\pi\epsilon} \text{diag}\left(\left[e^{-j\frac{2\pi}{Ma}\left(\frac{M_a}{4}+1-\frac{M_a}{2}k\right)\epsilon}, \cdots, \right. \right.$$
$$\left. \left. e^{-j\frac{2\pi}{Ma}\left(\frac{3M_a}{4}-\frac{M_a}{2}k\right)\epsilon} \right]\right) \times \quad (29)$$
$$\left(\mathbf{A}_\tau^0 \mathbf{d}[k] + \mathbf{A}_\tau^1 \mathbf{d}[k-1] \right) + \mathbf{A}^H \mathbf{w}[k],$$

for $k = L_{CP}, \cdots, N_c + L_{CP}$ and $0 \leq \tau < \frac{M}{2}$. The model described in this section can be extended to the general case where $\tau \geq \frac{M}{2}$. We just need to determine the number of full symbol periods in the delay. This is tantamount to computing $k_0 = \lfloor \frac{\tau}{M/2} \rfloor$. Then, the generalization reduces to

$$\mathbf{y}[k] = h e^{j2\pi\epsilon} \text{diag}\left(\left[e^{-j\frac{2\pi}{Ma}\left(\frac{M_a}{4}+1-\frac{M_a}{2}k\right)\epsilon}, \cdots, \right. \right.$$
$$\left. \left. e^{-j\frac{2\pi}{Ma}\left(\frac{3M_a}{4}-\frac{M_a}{2}k\right)\epsilon} \right]\right) \times \quad (30)$$
$$\left(\mathbf{A}_\tau^0 \mathbf{d}[k-k_0] + \mathbf{A}_\tau^1 \mathbf{d}[k-k_0-1] \right) + \mathbf{A}^H \mathbf{w}[k].$$

IV. PREAMBLE DESIGN

The aim of this section is to design a new random access signal, which is the main contribution of the paper. The most suitable preamble structure should simplify the preamble detection, without degrading the performance. A computationally simple method is based on comparing the peak of the correlation between the received preamble and the set of locally generated sequences with a given threshold. To reach a decision with the peak detector, it is crucial that the received preamble keeps the good correlation properties of the transmitted sequence. This section shows that the random access signal presented in [10] does not preserve the structure of the preamble, because phase jumps arise across multicarrier symbols. In addition, the AFB and the preamble detector have to be executed multiple times. These facts hinder the implementation of an efficient correlation-based preamble detector. To guarantee that the pruned DFT-s-FBMC scheme does not alter the structure of the transmitted preamble and allows fast preamble detection, this section demonstrates that the CP and the time-reversal technique are decisive. Towards this end, we start by analyzing the demodulated signal. Closely analyzing (30) we notice that the phase response of the channel is linear within $\mathbf{y}[k]$, while a phase jump arises between the last symbol of $\mathbf{y}[k]$ and the first symbol of $\mathbf{y}[k+1]$. According to Section II, the preamble sequence is split into N_c vector symbols that are indexed by $k = L_{CP}, \cdots, N_c + L_{CP} - 1$. If we plainly concatenate $\{\mathbf{y}[L_{CP}], \cdots, \mathbf{y}[N_c + L_{CP} - 1]\}$ to reconstruct the preamble sequence, then phase continuity is not preserved. To overcome this issue, which is crucial for successful preamble detection, vector symbols must be concatenated in a reversed order. Stacking column-wise the vectors as $\mathbf{y}_e = \left[\mathbf{y}^T[N_c + L_{CP} - 1], \cdots, \mathbf{y}^T[L_{CP}] \right]^T$, we can define a new system equation, namely,

$$\mathbf{y}_e = h e^{jc} \text{diag}\left(\left[e^{-j\frac{2\pi}{Ma}0\epsilon}, \cdots, e^{-j\frac{2\pi}{Ma}\left(\frac{M_a}{2}N_c-1\right)\epsilon} \right]\right) \mathbf{d}_e + \mathbf{w}_e, \quad (31)$$

where c is a constant term. The extended noise and data vectors are respectively defined as $\mathbf{w}_e = \left[\mathbf{w}^H[N_c + L_{CP} - 1]\mathbf{A}, \cdots, \mathbf{w}^H[L_{CP}]\mathbf{A} \right]^H$ and

$$\mathbf{d}_e = \begin{bmatrix} \mathbf{A}_\tau^0 \mathbf{d}[N_c + L_{CP} - 1 - k_0] + \mathbf{A}_\tau^1 \mathbf{d}[N_c + L_{CP} - 2 - k_0] \\ \vdots \\ \mathbf{A}_\tau^0 \mathbf{d}[L_{CP} - k_0] + \mathbf{A}_\tau^1 \mathbf{d}[L_{CP} - 1 - k_0] \end{bmatrix}. \quad (32)$$

The system model defined by (31) gives us some hints on the random access signal generation and the frame format. For instance, to allow fast detection, it becomes evident that the vector $\mathbf{d}_e$ must capture all preamble symbols to avoid adopting the sliding window approach. This is fulfilled if the preamble symbols are inserted within the time-frequency grid as follows

$$\mathbf{d}[N_c + L_{CP} - 1 - k] = \left[x_{u,v}\left(\left(k\frac{M_a}{2}\right) \text{mod} N_{ZC}\right), \cdots, \right.$$
$$\left. x_{u,v}\left(\left((k+1)\frac{M_a}{2} - 1\right) \text{mod} N_{ZC}\right) \right]^T, \quad (33)$$

for $k = 0, \cdots, N_c + L_{CP} - 1$. Notice that that the time-reversal technique is necessary at the transmitter. Let $x_{u,v}(n)$ denote the preamble sequence of length N_{ZC} that is generated after cyclically shifting by C_v positions the root sequence $x_u(n) = e^{-j\frac{\pi u n(n+1)}{N_{ZC}}}$, where $u = 1, \cdots, N_{ZC} - 1$. The cyclic shift C_v is picked from this set $\{0, 1, \cdots, N_{ZC} - 1\}$. It must be mentioned that the number of slots (N_c), the number of carriers (M_a) and the length of the preamble sequence (N_{ZC}) must satisfy $N_c \frac{M_a}{2} \geq N_{ZC}$. This constraint highlights that the symbol vectors $\{\mathbf{d}[0], \cdots, \mathbf{d}[L_{CP-1}]\}$ convey redundancy. It can be readily verified that the last τ_I symbol positions of
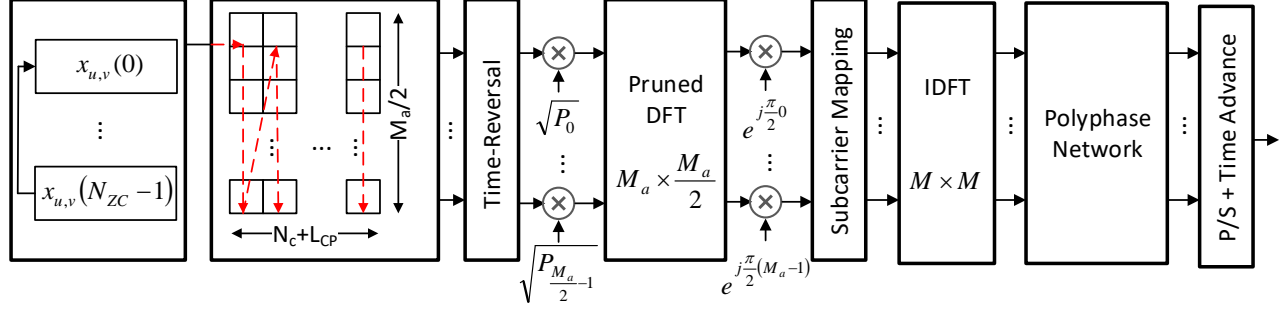
Fig. 1. FBMC-based PRACH transmitter block diagram.

$\mathbf{d}_e$ are filled in with the symbols that are shifted out of the sequence. By plugging (33) into (32), (31) becomes

$$
\begin{aligned}
\mathbf{y}_e = \ & he^{jc}\mathrm{diag}\Bigg(\Big[e^{-j\frac{2\pi}{M_a}0\epsilon}x_{u,v}\left(\tau_I\right),\cdots, \\
& e^{-j\frac{2\pi}{M_a}\left(\frac{M_a}{2}N_c-1\right)\epsilon}x_{u,v}\left(\left(N_c\frac{M_a}{2}-1+\tau_I\right)\mathrm{mod}N_{ZC}\right)\Big]\Bigg) \\
& +\mathbf{w}_e.
\end{aligned}
$$
(34)

The cyclic shift channel described in (34) holds true for $0 \leq \tau \leq L_{CP}\frac{M}{2}$ (or, equivalently, $0 \leq \tau_I \leq L_{CP}\frac{M_a}{2}$). Remarkably, we can conclude that the CP ensures the circular structure of the received preamble for $0 \leq \tau \leq \tau_{\mathrm{MAX}}$, as long as $L_{CP} > \lfloor\frac{\tau_{\mathrm{MAX}}}{M/2}\rfloor$. This condition links the preamble format to the maximum delay τ_{MAX}. To reduce the overhead to the highest possible extent, the size of the CP block is defined by

$$
L_{CP} = \left\lfloor\frac{\tau_{\mathrm{MAX}}}{M/2}\right\rfloor + 1.
$$
(35)

The CP also inhibits ISI between the PRACH and previous subframes. Note that the level of granularity to construct the CP block is governed by the number of carriers. The lower M, the finer the granularity.

It is worth mentioning that preamble sequences are characterized by the tuple (u, C_v). It is well known that if N_{ZC} is a prime number, then $x_{u_1,v_1}(n)$ and $x_{u_2,v_2}(n)$ are orthogonal, for $u_1 = u_2$ and $C_{v_1} \neq C_{v_2}$. When the sequences are generated from different root sequences, then orthogonality is not satisfied. In this case, the correlation between $x_{u_1,v_1}(n)$ and $x_{u_2,v_2}(n)$ is $\frac{1}{\sqrt{N_{ZC}}}$, for $u_1 \neq u_2$. Another interesting property of ZC sequences is that $x_{u,v}(n)$ can be expressed as function of the root sequence as follows:

$$
x_{u,v}(n) = x_u\left((n+C_v)\mathrm{mod}N_{ZC}\right) \propto x_u(n)e^{-j\frac{2\pi}{N_{ZC}}uC_vn}.
$$
(36)

It is important to remark that the burst formulated in (2) spans $(N_c + L_{CP} + 1)\frac{M}{2}$ samples. From the theory developed in [11], it can be proven that the energy of the first and last $\frac{M}{4}$ samples, which are located at the tail and the head of the burst, is considerably lower than the average power. Hence, the effective length is equal to $(N_c + L_{CP})\frac{M}{2}$ samples. To harness the improved time localization property of the pruned DFT-s-FBMC waveform, the time advance mechanism could be applied to the PRACH burst. The random access signal

generation is illustrated in Figure 1. First, symbol vectors are fed from a circular buffer whose content corresponds to the preamble sequence. An alternative interpretation could be the arrangement into a two-dimensional grid of a periodic extension of the preamble sequence. Then, a time reversal operation is performed. This task is equivalent to reverse the rows of the resulting matrix. Next, the random access signal is constructed by modulating the time-reversed symbol vectors onto the pruned DFT-s-FBMC waveform. Finally, the timing is adjusted to advance the transmission $\frac{M}{4}$ samples.

V. PREAMBLE DETECTOR

The objective of this section is to design a computationally efficient preamble detector. To this end, we build upon the preamble design described in Section IV. At the receive side, the scheme of the transmitter is reversed. The block diagram is shown in Figure 2. First of all the base station shifts the detection window $\frac{M}{2}L_{CP} - \frac{M}{4}$ samples, assuming that the time advance mechanism is applied. Then, the signal is fed into the AFB to decompose the subcarriers in the frequency domain. Next, the decoding matrix $\mathbf{PC}^H\mathbf{\Theta}^H$ is used to equalize the subcarriers that are allocated to the PRACH. At this stage, the system model can be represented as (14). Finally, time-reversal and concatenation operations are performed, leading to (34). By design, $N_c\frac{M_a}{2} \geq N_{ZC}$. Therefore, the first step to compute the decision variable is based on performing a matched filter operation on the first N_{ZC} elements of $\mathbf{y}_e$, leading to

$$
C_{\mathrm{MF},v}(n) = \begin{cases} [\mathbf{y}_e]_n x_v^*(n) & 0 \leq n \leq N_{ZC}-1 \\ 0 & n \geq N_{ZC}, \end{cases}
$$
(37)

for $1 \leq v \leq N_{ZC} - 1$. In order to detect the preamble and estimate the RTT, the output of the matched filter is transformed by means of the inverse discrete Fourier transform (IDFT) to the following metric

$$
\rho_{v\mu} = \sum_{k=0}^{L_{\mathrm{PDI}}-1} \left| \frac{\displaystyle\sum_{n=0}^{\frac{M_aN_c}{2L_{\mathrm{PDI}}}-1} C_{\mathrm{MF},v}\left(n+k\frac{M_aN_c}{2L_{\mathrm{PDI}}}\right) \times e^{j\frac{2\pi}{N_{\mathrm{IDFT}}}\left(n+k\frac{M_aN_c}{2L_{\mathrm{PDI}}}\right)\mu}}{N_{ZC}} \right|^2,
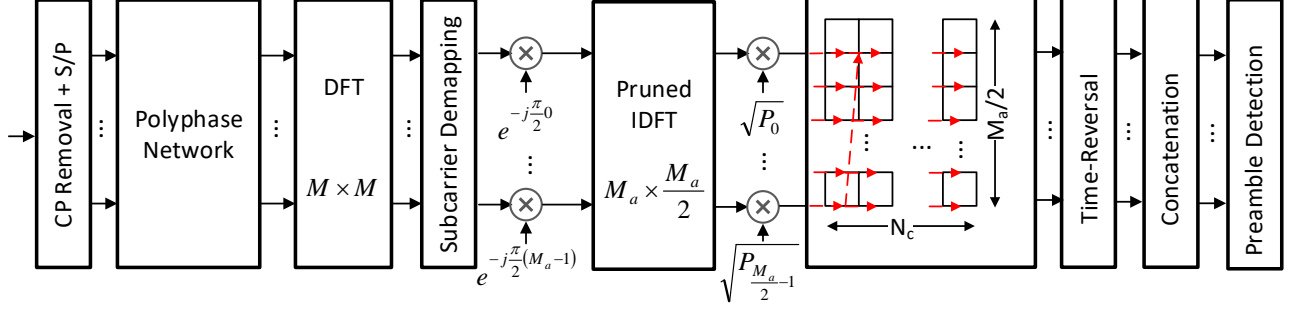$$
(38)

Fig. 2. FBMC-based PRACH receiver block diagram.

for $0 \le \mu \le N_{\text{IDFT}}-1$. The application of the matched filter and the IDFT are equivalent to computing the correlation between the received signal and a local sequence generated from the root v. We have derived a model that is sufficiently general to accommodate a full-length correlation detector ($L_{\text{PDI}} = 1$) and a non-coherent post detection integration (NCPDI) detector ($L_{\text{PDI}} > 1$). This is a significant improvement on the system presented in [10], which only supports NCPDI detectors. Concerning implementation aspects, selecting $N_{\text{IDFT}} > N_{\text{ZC}}$ allows us to increase the resolution of the estimation. Remarkably, if N_{IDFT} is a power of 2 and $L_{\text{PDI}} = 1$, the IFFT algorithm can be executed to compute the IDFT. Hence, to drastically reduce the number of arithmetic operations, in the rest of the section we stick to $L_{\text{PDI}} = 1$.

The correlation in (38) yields a small value when transmitted and local ZC sequences are generated from different roots. In the rest of the cases, the closed-form expression of (38) is written as

$$\rho_{u\mu} = \frac{|h|^2}{|N_{\text{ZC}}|^2} \left| \frac{\sin\left(\pi(\epsilon \frac{N_{\text{ZC}}}{M_a} + u(C_v + \tau_I) - \mu \frac{N_{\text{ZC}}}{N_{\text{IDFT}}})\right)}{\sin\left(\frac{\pi}{N_{\text{ZC}}}(\epsilon \frac{N_{\text{ZC}}}{M_a} + u(C_v + \tau_I) - \mu \frac{N_{\text{ZC}}}{N_{\text{IDFT}}})\right)} \right|^2 + \eta_{v\mu},$$

(39)

where $\eta_{v\mu}$ is the noise component. Without of loss of generality it has been assumed that the transmitted preamble is characterized by (u, C_v). In the most general case, where several replicas of the preamble are transmitted and the receiver is equipped with multiple antennas, the decision variable is obtained as a non-coherent summation, namely,

$$\rho_{u\mu} = \sum_{a=1}^{N_{\text{RX}}} \sum_{r=1}^{R} \rho_{u\mu}^{ar}.$$

(40)

The variables $\{\rho_{u\mu}^{ar}\}$ are obtained by computing the point-wise multiplication by $x_u^*(n)$ and executing the IFFT over the r-th replica received on the a-th antenna.

A. Peak search

The first step towards estimating the delay is to perform a peak search. The criterion that drives the peak detection is based on finding the correlation values that exceed a predefined

threshold. That is, if $\rho_{u\mu} \ge r_{\text{th}}$, then $\rho_{u\mu}$ is classified as a peak value. The detection threshold r_{th} is computed to comply with the target false alarm probability, which is denoted P_{FA}. In the event that no preamble is transmitted, the probability of $\rho_{u\mu} \ge r_{\text{th}}$ should be lower than P_{FA}, for any candidate sequence.

Bearing in mind the statistical information provided in Section II, we can resolve that the extended noise vector obeys this distribution $\mathbf{w}_e \sim \mathcal{CN}\left(\mathbf{0}_{\frac{N_c M_a}{2} \times \frac{N_c M_a}{2}}, \mathbf{I}_{\frac{N_c M_a}{2}}\right)$. Accordingly, the noise component in (40) can be expressed as $\eta_{v\mu} = \frac{1}{N_{\text{ZC}}} \chi^2(2RN_{\text{RX}})$, where $\chi^2(n)$ is distributed according to the chi-square distribution with n degrees of freedom. For single-user access, the equation that relates the false alarm probability to the threshold is derived as follows [22]:

$$P_{\text{FA}} = 1 - \left(1 - e^{-\frac{r_{\text{th}}N_{\text{ZC}}}{2}} \sum_{k=0}^{RN_{\text{RX}}-1} \frac{1}{k!} \left(\frac{r_{\text{th}}N_{\text{ZC}}}{2}\right)^k\right)^{D_w},$$

(41)

where D_w is the window search size [7]. The proposed method follows a window-based detection approach, where D_w is equal to the length of zero correlation zone, i.e. N_{CS}, which is provided by the network [15]. When there are N_U users in simultaneous access, the overall false alarm probability becomes $P_{\text{FA}}^{N_U} = 1 - (1 - P_{\text{FA}})^{N_U}$.

It can be deduced from (39) that the highest correlation value will be observed at the IDFT bin

$$\mu_p = \left\lfloor \left(\left(\epsilon \frac{N_{\text{ZC}}}{M_a} + u(C_v + \tau_I)\right) \bmod N_{\text{ZC}}\right) \frac{N_{\text{IDFT}}}{N_{\text{ZC}}} \right\rfloor,$$

(42)

when the transmitted preamble is characterized by (u, C_v).

B. TO estimation in low mobility scenarios

In the absence of CFO, the shifts τ_I and C_v can be unambiguously estimated from μ_p as long as there is a one-to-one correspondence between the position of the peaks and the delays. Essentially, this means that C_v must be picked from a subset that prevents different preamble sequences arriving at different time instants from exhibiting the same signature at reception. In this regard, to distinguish preamble correlation peaks, the shifts are selected as follows [15]:

$$C_v = vN_{\text{CS}}, \quad v = 0, \cdots, \left\lfloor \frac{N_{\text{ZC}}}{N_{\text{CS}}} \right\rfloor - 1.$$
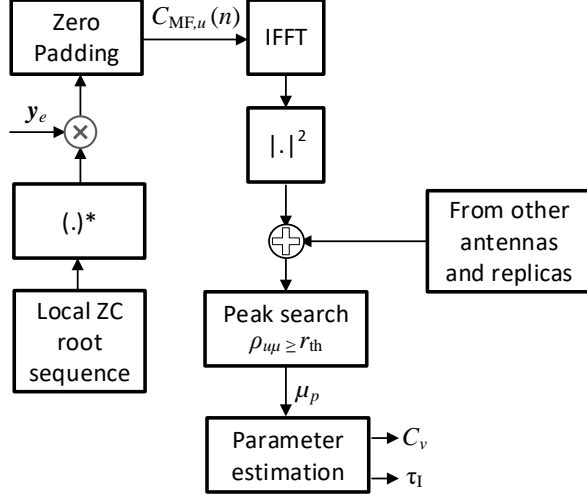
(43)

Fig. 3. Preamble detector.

In low mobility scenarios the spacing between candidate sequences is controlled by N_{CS}. The preamble design rules allow the receiver to resolve all possible time uncertainties, as long as $\tau_I < N_{CS}$. The schematic view of the detector is shown in Figure 3.

It is worth recalling that $\tau_I = \lfloor \tau \frac{M_a}{M} \rceil$, where τ is the RTT normalized to the sampling period T_s. Taking into account the granularity of time offered by the detector, the estimated delay can be computed as $\hat{\tau} = \frac{M}{M_a} \tau_I$. Assuming that τ_I is perfectly estimated from the peak values, the reliability of the estimator is such that $|\tau - \hat{\tau}| \leq 0.5 \frac{M}{M_a}$. Hence, the RTT can be estimated with a time resolution of $\frac{M}{M_a} T_s$, which is equivalent to $\frac{1}{M_a \Delta_f}$.

C. TO estimation in high mobility scenarios

When the CFO comes into play, attention must be drawn to the case $\epsilon = \pm n_\epsilon \frac{M_a}{N_{ZC}}$, where $n_\epsilon \in \mathbb{Z}$. In this particular situation, the CFO causes a cyclic shift that is equal to $d_{u n_\epsilon}$. That is, the peak emerges at

$$
\begin{aligned}
\mu_p &= \left\lfloor ((n_\epsilon + u(C_v + \tau_I)) \bmod N_{ZC}) \frac{N_{IDFT}}{N_{ZC}} \right\rfloor \\
&= \left\lfloor ((u(C_v + \tau_I + d_{u n_\epsilon})) \bmod N_{ZC}) \frac{N_{IDFT}}{N_{ZC}} \right\rfloor.
\end{aligned}
\tag{44}
$$

The variable $d_{u n_\epsilon}$ is computed by solving $n_\epsilon = u d_{u n_\epsilon} \bmod N_{ZC}$. All this indicates that in high mobility scenarios, further restrictions must be introduced to the preamble generation procedure. This has motivated the definition of the restricted preamble sets A and B [15]. The goal is to ensure that the effect of the CFO is not mistaken for any valid sequence.

It must be underlined that the estimator can deal with CFO values multiple of $\frac{M_a}{N_{IDFT}} \Delta_f$ just by performing additional hypothesis tests. To further understand this, we will initially focus on the case where there is no frequency misalignment.

Under this premise, the presence of a sequence that is characterized by (u, C_v) is determined by evaluating the IDFT outputs at

$$
\mu = \left\lfloor ((u(C_v + \tau_I)) \bmod N_{ZC}) \frac{N_{IDFT}}{N_{ZC}} \right\rfloor,
\tag{45}
$$

for $0 \leq \tau_I < N_{CS}$. At these positions, as evidenced from (39), the magnitude of $\rho_{u\mu}$ decreases in presence of CFO. In the worst case scenario, the preamble cannot be detected as correlation values fall below the threshold. To overcome this hurdle, the window search must be extended by including the indexes

$$
\mu = \left(\left\lfloor ((u(C_v + \tau_I)) \bmod N_{ZC}) \frac{N_{IDFT}}{N_{ZC}} \right\rfloor + n_\mu \right) \bmod N_{IDFT},
\tag{46}
$$

where $n_\mu \in \mathbb{Z}$. Remarkably, when $\epsilon = n_\mu \frac{M_a}{N_{IDFT}}$, the main lobe of the correlation will be centered at some grid point. If the length of the IDFT is sufficiently high, the estimator will not suffer any performance degradation because of the CFO. The additional grid points that need to be checked are dictated by the frequency resolution and the maximum normalized shift ϵ_{MAX}. Hence, $|n_\mu| \leq \lfloor \epsilon_{MAX} \frac{N_{IDFT}}{M_a} \rfloor$.

D. Comparison with SC-FDM

The analysis conducted in this section reveals that the proposed scheme is able to get an estimation of the TO with a time resolution of $\frac{1}{M_a \Delta_f}$. It is noteworthy to mention that the estimator is able to combat the adverse effects of the CFO with a frequency resolution of $\frac{M_a}{N_{IDFT}} \Delta_f$. Therefore, the resilience of the detector against the CFO is improved by increasing the IDFT length.

The detector in the SC-FDM counterpart can be efficiently implemented as well. Analogously to the procedure followed in this section, the delay can be estimated upon computing a point-wise multiplication of the demodulated signal with a root ZC sequence, followed by an IFFT [23], [24]. Thus, regardless of the multicarrier modulation format, the complexity of the detector is similar. The difference lies in the fact that in the SC-FDM context, the TO is estimated with a time resolution of $\frac{1}{N_{IDFT} \Delta_f}$. The negative impact of the CFO is compensated with a frequency resolution of Δ_f.

Remarkably, there exists a duality between the access schemes based on SC-FDM and FBMC. Both schemes have similar behaviour patterns in presence of the time and the frequency misalignment, with the exception that the roles played by the time and the frequency are exchanged. In FBMC-based (SC-FDM) access schemes, the TO (CFO) translates into a cyclic shift of the preamble sequence, while the CFO (TO) linearly shifts the phase of the preamble. For this reason, the IFFT has an impact on either the time or the frequency resolution, depending on the waveform design. The fine frequency resolution of the proposed detector could be leveraged to enhance the random access response (RAR) that is generated upon detecting the preamble. In 5G NR, the RAR inlcudes a timing correction. In addition, the RAR could comprise a frequency adjustment based on the estimated CFO. Then, the UE could update the not just the timing but also the

TABLE I
SYSTEM PARAMETERS

	SC-FDM	FBMC
Subcarriers	$M = 2048$	$M = 1024$
Active subcarriers	$M_a = 839$	$M_a = 420$
Subcarrier spacing	$\Delta_f = 1.25$ KHz	$\Delta_f = 2.5$ KHz
Frequency sampling	$f_s = 2.56$ MHz	$f_s = 2.56$ MHz
PRACH bandwidth	$B_{PRACH} = 1.08$ MHz	$B_{PRACH} = 1.08$ MHz
PRACH duration	$T_{PRACH} = 3$ ms	$T_{PRACH} = 3$ ms
Transmit antennas	$N_{TX} = 1$	$N_{TX} = 1$
UE antenna gain	$G_T = 0$ dBi	$G_T = 0$ dBi
Receive antennas	$N_{RX} = 1$	$N_{RX} = 1$
Satellite antenna G/T	$G_R/T = $ -4.9 dB K^{-1}	$G_R/T = $ -4.9 dB K^{-1}
Sequence repetitions	$R = 2$	$R = 2$
Carrier frequency	$f_c = 2$ GHz	$f_c = 2$ GHz
Beam diameter	28 km	28 km
Satellite altitude	600 km	600 km
Elevation angle	60º	60º

TABLE II
PRACH PARAMETERS

	SC-FDM	FBMC
Effective burst duration	$T_{SEQ} = 2284.37\mu s$	$T_{SEQ} = 2200\mu s$
Effective CP length	$T_{CP} = 684.37\mu s$	$T_{CP} = 600\mu s$
Effective guard time	$T_G = 715.63\mu s$	$T_G = 800\mu s$
Preamble length	$N_{ZC} = 839$	$N_{ZC} = 839$
Zero correlation zone	$N_{CS} = 100$	$N_{CS} = 100$

Fig. 4. Time response of the random access signal.

frequency before the next uplink transmission, which would significantly reduce ICI. The remaining steps of the random access procedure would remain the same.

With regards to the modulator and the demodulator, it becomes evident that the FBMC implementation comes at the cost of an increase of the complexity. There are two aspects explaining why FBMC is more demanding than SC-FDM in terms of complexity, i.e., the pulse shaping operation and the reduced symbol period. The complexity analysis conducted in [11] shows that the computational complexity of the pruned DFT-s-FBMC waveform is approximately two times higher than in SC-FDM.

VI. NUMERICAL RESULTS

In this section we evaluate the initial uplink synchronization method described in previous sections. The goal is to demonstrate that the FBMC waveform is an eligible technology component of forthcoming B5G-based LEO satellite communications. As a benchmark, we will consider the random access procedure adopted in [15] and the traditional preamble detection method detailed in [24]. In the rest of the section, we use the acronyms FBMC and SC-FDM to identify the proposed and the standardized access scheme, respectively. To shape the subcarrier signals, the FBMC system employs the time-frequency localization prototype pulse [20], [21]. The coefficients of the pulse are formulated in (26).

When the waveform of choice is FBMC, it would be desirable that the PRACH configuration defined in 5G NR could remain more or less intact. Clearly the objective is to ensure a high level of commonality across different waveforms. Following this approach, both SC-FDM and FBMC follow the procedure described in [15] to generate the preamble set.
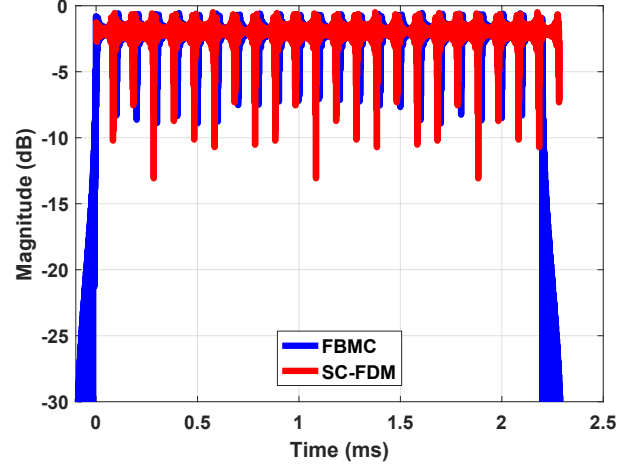
According to [15], the preambles can be grouped in two categories. The first category includes the preamble formats 0, 1, 2, 3, which use $\Delta_f = 1.25, 5$ kHz. The second category is formed by the preamble formats A1, A2, A3, B1, B2, B3, B4, C0, C2, which can be implemented with $\Delta_f = 15 \times 2^\mu$ kHz, with $\mu = 0, 1, 2, 3, 4, 5, 6$. It is important to remark that the sequences of the second category are not designed to target very large cell sizes. Indeed, the higher the value of Δ_f, the lower the cell size. This evidences that sequences of the second category are not suitable for satellite communication systems where beams are in the order of tens of km. Accordingly, we have selected the preamble format 1 with $\Delta_f = 1.25$ KHz, which is the preamble format that supports the highest cell size. Starting from the root index $u = 7$, 64 ZC preamble sequences are formed according to the restricted preamble set type B, which is created to establish uplink synchronization in high mobility scenarios. For the sake of fairness in the comparison, FBMC and SC-FDM are allocated the same time and frequency resources. However, as Table I shows, the numerology varies. The idea of reducing the number of carriers in FBMC is to offer more flexibility to configure the CP length. Thanks to this modification, FBMC is able to convey a slight modified version of the preamble format 1 on a resource unit that spans 3 ms and 1.08 MHz in the time-frequency plane. The details are gathered in Table II. The parameters of SC-FDM have been obtained from [15]. In 5G NR, the burst is formed by the CP and the preamble fields, which span 1600 μs and 684.37 μs, respectively. To transmit a similar burst format in the FBMC counterpart, we have followed the design guidelines reported in Section IV. The resulting burst is composed of 11 FBMC multicarrier symbols, of which $L_{CP} = 3$ are allocated to the CP and $N_c = 8$ are allocated to the preamble. Hence, the burst spans 2400 μs ($12\frac{M}{2}$ samples). However, the unique properties of the pruned DFT-s-FBMC modulation allows us to neglect the first and the last $\frac{M}{4}$ samples of the burst, as the energy mainly comes from the other samples. Accordingly, the effective length of the burst is $2200\mu s$. This feature is exploited by starting the transmission $100\mu s$ ($\frac{M}{4}$ samples) before the beginning of the
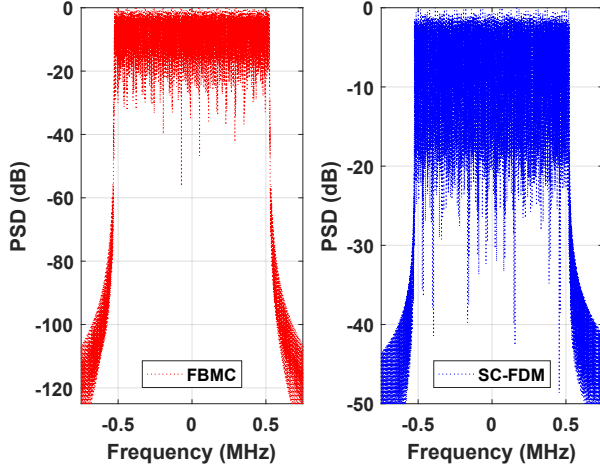
Fig. 5. PSD of the random access signal.

Fig. 6. Missed detection probability versus SNR in SC-FDM and FBMC.

PRACH slot, resulting in weak interference with the previous subframe. The time advance mechanism together with the good time localization property of the waveform offers the possibility to extend the guard time up to $800\mu s$. Another distinctive feature of the proposed access scheme stems from the overhead transmitted ahead of the preamble, which acts similarly as a CP of $L_{CP}\frac{M}{2}$ samples will do in SC-FDM. Bearing in mind this analogy, the effective CP length in FBMC becomes $600\mu s$.

A. Time response

This subsection focuses on verifying that the effective burst duration matches the values of Table II. To this end, we have represented in Figure 4 the time response of the random access signal over the interval $[-0.1ms \quad 2.5ms]$. As Figure 4 shows, a negative offset of 100 μs can be applied to the FBMC burst without significantly increasing the leakage towards previous subframes. The figure also corroborates that in FBMC the energy of the burst is confined within an interval that approximately spans 2.2 ms. In alignment with Table II, the duration is slightly increased in SC-FDM. In conclusion, the FBMC plot corroborates that the proposed random access signal fits in the time window that corresponds to a random access occasion.

B. Frequency response

In this subsection we aim at showing that FBMC exhibits better spectral confinement than SC-FDM. To evaluate the frequency domain information, Figure 5 depicts the power spectral density (PSD) of both modulations in a 1.5 MHz bandwidth. For the sake of the clarity, the highest spectral peak is normalized to 0 dB. This normalization allows us to clearly see that that FBMC achieves larger spectral leakage suppression than SC-FDM outside the PRACH bandwidth.

C. Missed detection probability

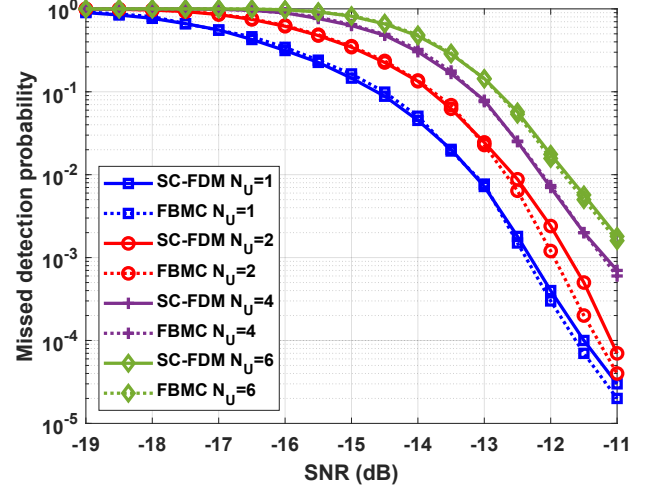To complete the performance analysis we evaluate the MDP in single and multi-user scenarios. The position of the UEs

are assumed to be uniformly located within the spotbeam area. The transmission goes through a flat fading channel with AWGN. This channel model is suitable for satellite communications, where the line-of-sight (LoS) component clearly dominates over the multipath effect. The events that lead to an erroneous detection include the detection of different preamble than the one that was sent, not detecting a preamble at all or correct preamble detection but with the wrong timing estimation. To comply with the performance requirements of the PRACH test defined in [25], a timing estimation error must be declared if the magnitude of the error is larger than 1.04 μs.

According to the NCS value gathered in Table II, the maximum RTT shall not exceed 94.28 μs. This configuration can be applied to a regenerative satellite architecture assuming that the pre-compensation mechanism is applied at the satellite payload side. Under this premise, it can be verified that the satellite beam diameter shall not exceed 28 Km and that the residual Doppler shift in the initial uplink synchronization can take values between -2.4KHz and 2.4KHz, for the parameters gathered in Table I. It is worth emphasizing that in the initial uplink transmission the frequency misalignment is approximately two times the residual Doppler shift in the downlink, which is computed with the analytical expressions provided in [26]. It must be mentioned that the range $[-2.4, \quad 2.4]$ KHz accommodates all differential Doppler values over the beam with respect to the reference point. For convenience, the center of the beam has been selected as the reference point. The maximum difference is observed at the edges of the beam, when the satellite is closest to the center of the beam.

In the detection scheme depicted in Figure 3, the detection threshold r_{th} is computed fixing the false alarm probability to 10^{-3}. To achieve a good compromise between the computational complexity and the estimation accuracy, the length of the IDFT is set to $N_{IDFT} = 2048$. The findings of Section V reveal that the preamble detector operates with a time resolution of 952 ns and a frequency resolution of 512 Hz, for the system parameters of Table I. Keeping the same parameters
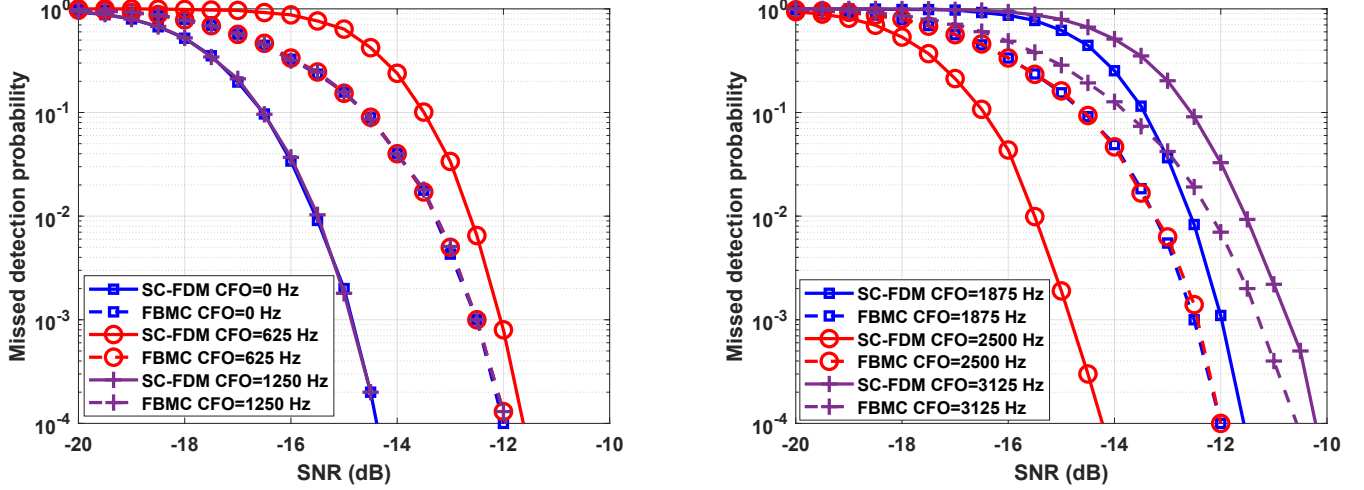
Fig. 7. Missed detection probability versus SNR in SC-FDM and FBMC for different values of CFO.

unchanged, the preamble detector devised for SC-FDM in [23], [24] offers a time resolution of 390 ns and a frequency resolution of 1.25 Hz. This allows us to create two rectangular lattices in the time-frequency plane, where the separation of adjacent points depend on the time ad frequency resolution. When the time and the frequency offset coincide with a lattice point, the performance of the detector is maximized, because the correlation value takes its maximum. In the rest of the cases, the detector must reach a decision that is not based on the correlation peak, but on a lower correlation value. Notice that $\frac{952}{390} = \frac{1250}{512}$. Therefore, the latency density is the same in both modulations. This observation highlights that on average the detector in SC-FDM and pruned DFT-s-FBMC modulations should achieve similar performance.

Concerning the comparison between the two contenders, we have represented in Figure 6 the MDP versus the SNR. The SNR is function of the satellite channel gain, the power of the symbols and the power of the noise, i.e., SNR = $|h|^2 \mathbb{E}\left\{|d_m[k]|^2\right\}$. In the proposed scenario, the CFO is uniformly drawn from $[-3.125,\ 3.125]$ KHz. The interval is broader than the uncertainty range caused by residual Doppler frequency shift. The objective is to also encompass possible local oscillator errors and frequency shifts owing to the user mobility. From figure 6 we can infer that FBMC and SC-FDM achieve similar performance. Predictably, with the increase in the number of active UEs, the MDP increases. It is worth highlighting that the preambles are not orthogonal when they are generated from different root sequences. Therefore, the interference among active UEs is the major cause of performance degradation. In Figure 6 we analyze the case in which UEs pick different preambles and thus, there are no collisions. In the scenario under study, when a given UE selects a sequence, the collision probability is given by $P_c = 1 - (1 - 1/64)^{N_U-1}$. Interestingly, the occurrence of collisions and missed-detection can be jointly evaluated through the success probability $P_s = (1 - P_c)(1 - \text{MDP})$. In accordance with the curves depicted in Figure 6, we can presume that FBMC and SC-FDM will practically achieve the same success probability.

To attain a more clear understanding of the performance results, we have presented in Figure 7 the MDP as function of the SNR for different CFO values. In SC-FDM, the granularity of the detector allows us to compensate the CFO perfectly, as long as it is a multiple of Δ_f. It is for this reason that for CFO={1.25, 2.5} KHz, the degradation is negligible and thus, the results coincide with CFO= 0 Hz. In the rest of the cases, the MDP is increased. In FBMC, the curves for CFO={0, 625, 1250, 1875, 2500} Hz are nearly matched. Clearly, FBMC benefits from a finer frequency granularity in presence of CFO. Comparing FBMC and SC-FDM, we can resolve that SC-FDM shows superior performance when the CFO is perfectly compensated. When the detector solely has to deal with the time uncertainty, SC-FDM achieves the lowest MDP, as it exhibits a finer time resolution than FBMC. In contrast, when the CFO is a fractional number of Δ_f, FBMC gives better results. In alignment with this observation, FBMC is able to guarantee access with higher reliability than SC-FDM, in the extreme case of CFO=3.125 KHz. In conclusion, SC-FDM and FBMC behave differently in presence of time and frequency offsets.

In order to conduct a more in-depth analysis, we have computed the minimum SNR that is required to achieve a MDP of 1%, for different CFO and TO values. This performance evaluation sheds light on how FBMC and SC-FDM resolve time and frequency uncertainties. The SNR values in the upper plot of Figure 8 have been obtained by fixing the CFO to the target value and modelling the TO as a discrete uniform distribution on $\{0, 1/f_s, \cdots, 241/f_s\}$. The set of possible TO values is determined by the sampling period and the beam size. The first conclusion that can be drawn from the upper plot of Figure 8 is that SC-FDM achieves the best and the worst results when the CFO is a multiple of Δ_f and $0.5\Delta_f$, respectively. In FBMC, the SNR hardly fluctuates and thus, it can be considered constant in almost all the CFO range. For CFO values higher than 3 KHz, the performance of SC-FDM degrades drastically, while FBMC exhibits stronger
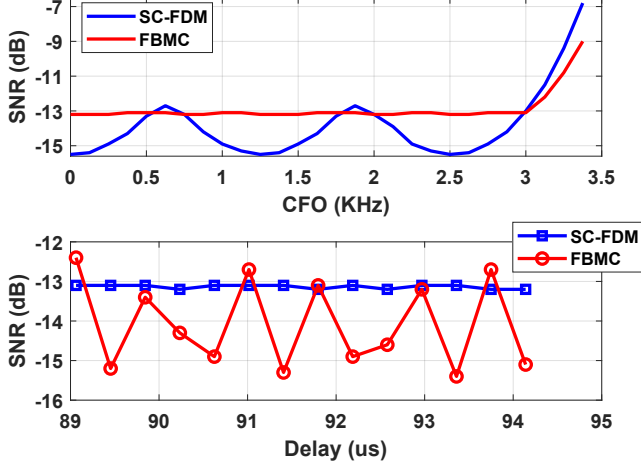
Fig. 8. Minimum SNR for different CFO and TO values in SC-FDM and FBMC at MDP=0.01.

immunity to CFO. For CFO> 3.375 KHz, neither SC-FBMC nor FBMC are able to meet the requirement that the MDP is equal or lower than 0.01. The performance is dictated by the normalized CFO with respect to the subcarrier spacing. Hence, by increasing (reducing) the subcarrier spacing, the maximum CFO that is tolerated will increase (decrease) as well. In the lower plot of Figure 8 we draw the attention to the time misalignment. Hence, for a given TO, the CFO is uniformly distributed on $[-3.125, \ 3.125]$ KHz. In order to facilitate interpretation of the results, we have analyzed a short interval. The SNR curve reveals that FBMC achieves the best and the worst performance when the TO is a multiple of $\frac{1}{M_a \Delta_f}$ and $0.5 \frac{1}{M_a \Delta_f}$, respectively. Notice that the TO does not always coincide with a maximum or a minimum, since $0.5 \frac{1}{M_a \Delta_f}$ is not a multiple of f_s. In SC-FDM, the SNR remains almost flat. Closely analyzing Figure 8 we can establish a CFO-TO duality, in the sense that the SC-FDM behaves in the time (frequency) domain similarly to FBMC in the frequency (time) domain. This duality is useful to investigate the application of FBMC and SC-FDM in a variety of satellite scenarios.

VII. CONCLUSIONS

In this paper we have investigated the enhancement of the initial uplink synchronization to allow direct LEO satellite access. The main impairment is the high CFO that results from the orbital motion. Contrary to the approach taken by other works, the solution that is proposed to improve the robustness to CFO focuses on the waveform rather than the preamble design. Motivated by its good time and frequency localization properties and its low envelope fluctuation, we have adopted the pruned DFT-s-FBMC waveform to convey the preamble. The analysis conducted in the paper reveals that the proposed design is suitable for LEO satellite communication systems, as it preserves the remarkable properties of the pruned DFT-s-FBMC waveform and facilitates the implementation of a computationally efficient detector. In addition, the random access signal presented in this paper achieves a high level

of commonality with 5G NR, because allows the system to inherit the preamble generation method and the time-frequency allocation pattern. In comparison to the standardized access scheme based on SC-FDM, the proposed solution gives better performance in many aspects. It exhibits much lower OOB emissions and achieves lower MDP in presence of very high CFO. Regarding the preamble detector, in both SC-FDM and pruned DFT-s-FBMC, the complexity is similar.

Future work may analyse the impact of the multi-path effect on the MDP, which is bound to arise when the UE is located at a densely built city or has a small elevation angle.

APPENDIX A

Closely analyzing (11), we can determine that the function

$$f_M[n] = \frac{\sin\left(\pi\left(\frac{M_a}{M}n + m\right)\right)}{\sin\left(\frac{\pi}{M_a}\left(\frac{M_a}{M}n + m\right)\right)} e^{j\frac{\pi}{M_a}\left(\frac{M_a}{M}n + m\right)} \quad (A.1)$$

has a better time localization than the pulse and the CFO component. It is assumed that only $2I + 1$ out of M terms of $f_M[n]$ contribute significantly. Particularly, those terms centered around $n_m = M - \lfloor m\frac{M}{M_a}\rfloor$. Therefore, the pulse and the CFO component can be treated as constant terms in $n \in [n_m - I, \ n_m + I]$, if $2I + 1 << M/\epsilon$. It can be verified that the energy of $f_M[n]$ is concentrated in the main lobe and eight adjacent side lobes. Accordingly, $I = \lceil \frac{M}{M_a}5\rceil$. Then, the feasibility condition can be recast as $\epsilon << M_a/10$. Under this premise, (11) reduces to

$$\xi_m^l \approx e^{j\frac{2\pi}{M}n_m\epsilon} p[n_m] p\left[n_m - \tau + l\frac{M}{2}\right] \times$$
$$\sum_{i=-I}^{I} H\left(i + m\frac{M}{M_a} - \lfloor m\frac{M}{M_a}\rceil\right), \quad (A.2)$$

where

$$H(i) = \frac{\sin\left(\pi\frac{M_a}{M}i\right)}{\sin\left(\frac{\pi}{M}i\right)} e^{j\frac{\pi}{M}i}. \quad (A.3)$$

Notice that $H(i)$ represents the DFT of the sequence

$$h[n] = \left\{ \underbrace{1, \cdots, 1}_{M_a/2}, \underbrace{0, \cdots, 0}_{M-M_a}, \underbrace{1, \cdots, 1}_{M_a/2} \right\} \quad (A.4)$$

evaluated on the radial frequency $\frac{2\pi}{M}i$. Knowing that $\left|\lfloor m\frac{M}{M_a}\rceil - m\frac{M}{M_a}\right| \leq 0.5$, it follows that the energy of $H\left(i + m\frac{M}{M_a} - \lfloor m\frac{M}{M_a}\rceil\right)$ is mainly distributed within $\left[-\frac{2\pi}{M}I \ \ \frac{2\pi}{M}I\right]$. According to this observation, together with the inverse DFT definition, we can state that the summation in (A.2) gives a good approximation to $\left\{Mh[n]e^{-j\frac{2\pi}{M}\left(m\frac{M}{M_a} - \lfloor m\frac{M}{M_a}\rceil\right)n}\right\}$ at $n = 0$. Another important finding is that for large M, $e^{j\frac{2\pi}{M}n_m\epsilon}$ tends to $e^{j2\pi\epsilon}e^{-j\frac{2\pi}{M_a}m\epsilon}$. In light of these observations, we can express (A.2) as

$$\xi_m^l \approx e^{j2\pi\epsilon}e^{-j\frac{2\pi}{M_a}m\epsilon} p[n_m] p\left[n_m - \tau + l\frac{M}{2}\right] M. \quad (A.5)$$

The last derivation step that is applied to simplify (A.2) relies on the fact that the pulse exhibits smooth variations with time, which allows us to establish that

$$
\begin{aligned}
p\left[n_{m+\tau_I}\right] &= p\left[M - \left\lfloor (m+\tau_I)\frac{M}{M_a}\right\rceil\right] \\
&= p\left[M - \left\lfloor \left(m+\left\lfloor \tau\frac{M_a}{M}\right\rceil\right)\frac{M}{M_a}\right\rceil\right] \\
&= p\left[M - \left\lfloor (m+\delta)\frac{M}{M_a}\right\rceil - \tau\right] \\
&\approx p\left[M - \left\lfloor m\frac{M}{M_a}\right\rceil - \tau\right].
\end{aligned}
\tag{A.6}
$$

where $|\delta| \leq 0.5$. Hence, $p\left[n_m - \tau\right]$ is almost identical to $p\left[n_{m+\tau_I}\right]$. Incorporating the aforementioned concepts and approximations, the eigenvalues read as

$$
\xi_m^l \approx e^{j2\pi\epsilon}e^{-j\frac{2\pi}{M_a}m\epsilon}p\left[n_m\right]p\left[n_{m+\tau_I}+l\frac{M}{2}\right]M.
\tag{A.7}
$$

Following the same rationale, we assert that (12) can be approximated to

$$
\lambda_m^l \approx p\left[n_m\right]p\left[n_m + l\frac{M}{2}\right]M.
\tag{A.8}
$$

APPENDIX B

First, we highlight that $\mathbf{H}_{\mathrm{T}}[-1] = \mathbf{0}_{\frac{M_a}{2}\times\frac{M_a}{2}}$ if $\tau_I = 0$ and $\tau_f = 0$. This result is evidenced from (20) and (22). To resolve the proof for the rest of the cases where $\tau_I > 0$ and $\tau_f = 0$, we recall that $n_m = M - \left\lfloor m\frac{M}{M_a}\right\rceil$ and $p[n] = 0$, for $n \notin \{0, \cdots, M-1\}$. Bearing this in mind, it can be verified that $p\left[n_{m+\tau_I} - \frac{M}{2}\right] = 0$, for $3\frac{M_a}{4} - \tau_I + 1 \leq m \leq 3\frac{M_a}{4}$ and $1 \leq \tau_I < \frac{M_a}{2}$. Then, it follows that $\xi_{3\frac{M_a}{4}-\tau_I+1}^{-1} = \cdots = \xi_{3\frac{M_a}{4}}^{-1} = 0$. The immediate consequence is that $\mathbf{H}_{\mathrm{T}}[-1] = \mathbf{0}_{\frac{M_a}{2}\times\frac{M_a}{2}}$.

APPENDIX C

Assuming that (24) and (25) hold true, the ratio of the channel eigenvalues can be expressed in the form of

$$
\frac{\xi_m^0}{\sqrt{\lambda_{m+\tau_I}^0 \lambda_m^0}} = e^{j2\pi\epsilon}e^{-j\frac{2\pi}{M_a}m\epsilon},
\tag{C.1}
$$

for $m = \frac{M_a}{4} + 1, \cdots, 3\frac{M_a}{4} - \tau_I$. Interestingly, in the rest of subcarriers we can establish this relation

$$
\frac{\xi_m^1}{\sqrt{\lambda_{m-\frac{M_a}{2}+\tau_I}^0 \lambda_m^0}} = e^{j2\pi\epsilon}e^{-j\frac{2\pi}{M_a}m\epsilon},
\tag{C.2}
$$

for $m = 3\frac{M_a}{4} - \tau_I + 1, \cdots, 3\frac{M_a}{4}$. The main conclusion is that the CFO yields a linear phase rotation across subcarriers, namely,

$$
\mathbf{D}_{\mathrm{T}} = e^{j2\pi\epsilon}\mathrm{diag}\left(\left[e^{-j\frac{2\pi}{M_a}\left(\frac{M_a}{4}+1\right)\epsilon}, \cdots, e^{-j\frac{2\pi}{M_a}\left(\frac{3M_a}{4}\right)\epsilon}\right]\right).
\tag{C.3}
$$

The structure of $\mathbf{D}_{\mathrm{T}}$ corroborates that the non-zero entries of the channel matrix have constant magnitude.

ACKNOWLEDGMENT

REFERENCES

[1] "3rd Generation Partnership Project; Technical Specification Group Radio Access Network; Solutions for NR to support non-terrestrial networks (NTN); (Release 16)." 3GPP TR 38.821.

[2] A. Guidotti, A. Vanelli-Coralli, T. Foggi, G. Colavolpe, M. Caus, J. Bas, S. Cioni, and A. Modenini, "LTE-based satellite communications in LEO mega-constellations," *International Journal of Satellite Communications and Networking*, vol. 37, no. 4, pp. 316–330, 2019.

[3] "3rd Generation Partnership Project; Technical Specification Group Radio Access Network; Study on New Radio (NR) to support non terrestrial networks; (Release 15)." 3GPP TR 38.811.

[4] G. Cui, Y. He, P. Li, and W. Wang, "Enhanced Timing Advanced Estimation With Symmetric Zadoff-Chu Sequences for Satellite Systems," *IEEE Communications Letters*, vol. 19, no. 5, pp. 747–750, 2015.

[5] P. Li, Y. He, G. Cui, W. Wang, and Y. Zhang, "A novel timing advanced estimation algorithm for eliminating frequency offset in satellite system," in *2015 IEEE 26th Annual International Symposium on Personal, Indoor, and Mobile Radio Communications (PIMRC)*, 2015, pp. 1792–1796.

[6] G. Schreiber and M. Tavares, "5G New Radio Physical Random Access Preamble Design," in *2018 IEEE 5G World Forum (5GWF)*, 2018, pp. 215–220.

[7] L. Zhen, H. Qin, B. Song, R. Ding, X. Du, and M. Guizani, "Random Access Preamble Design and Detection for Mobile Satellite Communication Systems," *IEEE Journal on Selected Areas in Communications*, vol. 36, no. 2, pp. 280–291, 2018.

[8] L. Zhen, A. K. Bashir, K. Yu, Y. D. Al-Otaibi, C. H. Foh, and P. Xiao, "Energy-Efficient Random Access for LEO Satellite-Assisted 6G Internet of Remote Things," *IEEE Internet of Things Journal*, vol. 8, no. 7, pp. 5114–5128, 2021.

[9] L. Zhen, T. Sun, G. Lu, K. Yu, and R. Ding, "Preamble Design and Detection for 5G Enabled Satellite Random Access," *IEEE Access*, vol. 8, pp. 49 873–49 884, 2020.

[10] M. Caus, A. I. Pérez-Neira, J. Bas, and L. Blanco, "New Satellite Random Access Preamble Design Based on Pruned DFT-Spread FBMC," *IEEE Transactions on Communications*, vol. 68, no. 7, pp. 4592–4604, 2020.

[11] R. Nissel and M. Rupp, "Pruned DFT-Spread FBMC: Low PAPR, Low Latency, High Spectral Efficiency," *IEEE Transactions on Communications*, vol. 66, no. 10, pp. 4811–4825, 2018.

[12] P. Siohan, C. Siclet, and N. Lacaille, "Analysis and design of OFDM/OQAM systems based on filterbank theory," *IEEE Transactions on Signal Processing*, vol. 50, no. 5, pp. 1170–1183, 2002.

[13] P. Singh, H. B. Mishra, A. K. Jagannatham, K. Vasudevan, and L. Hanzo, "Uplink Sum-Rate and Power Scaling Laws for Multi-User Massive MIMO-FBMC Systems," *IEEE Transactions on Communications*, vol. 68, no. 1, pp. 161–176, 2020.

[14] S. Srivastava, P. Singh, A. K. Jagannatham, A. Karandikar, and L. Hanzo, "Bayesian Learning-Based Doubly-Selective Sparse Channel Estimation for Millimeter Wave Hybrid MIMO-FBMC-OQAM Systems," *IEEE Transactions on Communications*, vol. 69, no. 1, pp. 529–543, 2021.

[15] "3rd Generation Partnership Project; Technical Specification Group Radio Access Network; NR; Physical channels and modulation; (Release 17)." 3GPP TS 38.211.

[16] Z. Y. Choi and Y. Lee, "Frame synchronization in the presence of frequency offset," *IEEE Transactions on Communications*, vol. 50, no. 7, pp. 1062–1065, 2002.

[17] Y. Liu, H. Yu, F. Ji, F. Chen, and W. Pan, "Robust Timing Estimation Method for OFDM Systems With Reduced Complexity," *IEEE Communications Letters*, vol. 18, no. 11, pp. 1959–1962, 2014.

[18] M. Caus, A. Perez-Neira, and E. Mendez, "Smart Beamforming for Direct LEO Satellite Access of Future IoT," *Sensors*, vol. 21, no. 14, 2021.

[19] A. Guidotti, C. Amatetti, F. Arnal, B. Chamaillard, and A. Vanelli-Coralli, "Location-Assisted Precoding in 5G LEO Systems: Architectures and Performances," in *European Conference on Networks and Communications (EuCNC) and the 6G Summit*, 2022.

[20] J. Nadal, C. A. Nour, and A. Baghdadi, "Design and Evaluation of a Novel Short Prototype Filter for FBMC/OQAM Modulation," *IEEE Access*, vol. 6, pp. 19 610–19 625, 2018.

[21] D. Pinchon and P. Siohan, "Derivation of analytical expressions for flexible PR low complexity FBMC systems," in *21st European Signal Processing Conference (EUSIPCO 2013)*, 2013.

[22] C. Rohde, N. Alagha, R. De Gaudenzi, H. Stadali, and G. Mocker, "Super-framing: a powerful physical layer frame structure for next generation satellite broadband systems," *International Journal of Satellite Communications and Networking*, vol. 34, no. 3, pp. 413–438, 2016.

[23] G. Wu, H. Yuan, W. Guo, S. Hu, and S. Li, "On design of physical random access channel in high-speed railway LTE systems," *Chinese Science Bulletin*, vol. 59, no. 35, pp. 5042–5050, Dec 2014.

[24] Tianhao Li, Wenbo Wang, and Tao Peng, "An improved preamble detection method for LTE PRACH in high-speed railway scenario," in *2015 10th International Conference on Communications and Networking in China (ChinaCom)*, 2015, pp. 544–549.

[25] "3rd Generation Partnership Project; Technical Specification Group Radio Access Network; NR; Evolved Universal Terrestrial Radio Access (EUTRA); Base Station (BS) radio transmission and reception (Release 17)." 3GPP TS 38.104.

[26] I. Ali, N. Al-Dhahir, and J. E. Hershey, "Doppler characterization for LEO satellites," *IEEE Transactions on Communications*, vol. 46, no. 3, pp. 309–313, 1998.

Màrius Caus received the M.Sc. and PhD (cum laude) degrees in Telecommunications engineering from the Universitat Politècnica de Catalunya (UPC), Barcelona, Spain, in July 2008 and December 2013, respectively. In 2009 he was granted by the Spanish Government to carry out his PhD studies in the Signal Theory and Communications Department at UPC. In 2018 he received the 2-year postdoctoral Juan de la Cierva fellowship from the Spanish Government. He has participated in several projects funded by the European Commission, the European Space Agency and the Spanish Ministry of Science. He is currently a Researcher at Centre Tecnològic de Telecomunicacions de Catalunya (CTTC), Castelldefels, Spain. His main research interests include filter bank based multicarrier systems, signal processing for communications and satellite communications.

Ana I. Pérez-Neira (SM'02, FM'20) is full professor at Universitat Politècnica de Catalunya in the Signal Theory and Communication department since 2006 and was Vice rector for Research (2010-14). Currently, she is the Director of Centre Tecnològic de Telecomunicacions de Catalunya, Spain. Her research is in signal processing for communications, focused on satellite communications. She has more than 60 journal papers and 300 conference papers. She is co-author of 7 books. She has leaded more than 20 projects and holds 8 patents. She is coordinator of the Networks of Excellence on satellite communications, financed by the European Space Agency: SatnexIV-V. She has been associate editor of the IEEE TSP and EURASIP SP and ASP. Currently she is senior area editor of IEEE OJSP. She is member of the BoG of the IEEE SPS and Vice-President for conferences (2021-23). She is IEEE Fellow and member of the Real Academy of Science and Arts of Barcelona (RACAB). She is recipient for the 2018 EURASIP Society Award and she has been the general chair of IEEE ICASSP'20 (the first big IEEE virtual conference held by IEEE with more than 15.000 attendees). In 2020, she has been awarded the ICREA Academia distinction by the Catalan government.